PNAS

www.pnas.org

Supplementary Information for

Carrier localization in perovskite nickelates from oxygen vacancies

Michele Kotiuga, Zhen Zhang, Jiarui Li, Fanny Rodolakis, Hua Zhou, Ronny Sutarto, Feizhou He, Qi Wang, Yifei Sun, Ying Wang, Neda Alsadat Aghamiri, Steven Bennett Hancock, Leonid P. Rokhinson, David P. Landau, Yohannes Abate, John W. Freeland, Riccardo Comin, Shriram Ramanathan, Karin M. Rabe

Michele Kotiuga

Email: mkotiuga@physics.rutgers.edu

This PDF file includes:

Supplementary Text

Description. This text contains detailed descriptions of the (1) experimental characterization techniques; (2) electrical transport mechanisms in SNO from resistivity versus temperature fitting; (3) Monte Carlo simulations; and, (4) solid-state oxygen-deficient perovskite nickelate resistive switches.

(1) Experimental characterization techniques

Electrical property characterization

Electrical resistance of samples after LPO2 annealing was measured on a temperature-controlled probe station by monitoring voltage-current curve while sweeping the voltage from -0.1 V to 0.1 V with a Keithley 2635A source meter. Pt electrodes were fabricated on the top of the films as contacts.

Electrical transport measurements below room temperature were conducted in a Quantum Design physical properties measurement system (PPMS) using a small excitation AC signal. For this transport measurement, 60 nm $SmNiO_3$ thin films were grown on (0001) sapphire substrate. The oxygen deficient SNO sample was obtained by annealing in LPO2 at 400 °C for 1 h.

Optical spectrum measurements

The optical transmission spectrum of samples after LPO2 annealing was measured with PerkinElmer Lambda 950 UV-VIS-NIR spectrophotometer in the wavelength range from 250 to 2000 nm with a resolution of 1 nm. Two-side polished LAO substrates were used for these measurements. Bare LAO substrate was utilized as a reference to extract the transmittance of SNO thin films.

Midinfrared nano-imaging

The midinfrared nano-imaging experiments were carried out in a commercial s-SNOM (neaspec GMBH). A cantilevered AFM tip with $R \approx 20$ nm apex radius coated with Pt oscillates at a frequency of $\Omega \approx 280$ kHz and tapping amplitude of ~100 nm. The tip is illuminated by a monochromatic quantum cascade laser beam at λ=10.5 μm at angle of 45° to the sample surface. The scattered light from tip and sample interface is demodulated at higher harmonics of tip resonance frequency and detected using phase modulation (pseudo-heterodyne) interferometry rendering simultaneous topography and near-field optical images.

X-ray diffraction measurements

The evolution of crystal structure of SNO after LPO2 annealing was studied by X-ray diffraction using Panalytical MRD X'Pert Pro high-resolution diffractometer with Cu *K*α radiation.

X-ray photoelectron spectroscopy

Photoelectron spectroscopy was conducted at beamline 29-ID IEX at the Advanced Photon Source, Argonne National Laboratory. The beamline uses an electromagnetic undulator providing

soft x-ray from 250 eV to 3000 eV; it is equipped with a variable line spacing plane grating monochromator and a Scienta R4000 hemispherical analyzer resulting in an overall energy resolution of 300 meV at 1500 eV incident energy. The geometry of the analysis chamber uses the so-called magic angle (55 degree between the detector and the photon beam) and data were collected in normal emission in a pressure better that 5×10^{-10} Torr.

Additional XPS analyses comparing hydrogenated and oxygen deficient $SmNiO_3$ were conducted with Kratos X-ray Photoemission Spectrometer using monochromatic Al $K\alpha$ x-ray beam (1486.6 eV). The binding energy of XPS spectrum was calibrated using C 1s photoemission peak at 284.6 eV. The oxygen deficient SNO is obtained by annealing in LPO2 at 450 ^{o} C for 1 h. A reference HSNO sample was obtained by electrochemical protonation in 0.1 M KOH by applying bias potential of -1.0 V (vs. Ag/AgCl) for 6 min.

X-ray absorption spectroscopy

XAS was performed at beamline 10ID-2 (REIXS) of the Canadian Light Source (47). The absorption was measured by total fluorescence yield with linearly polarized photons, and in normal incidence geometry. The electric field vector is parallel to (110) direction in pseudocubic coordinate system. For XAS measurements, 50 nm $NdNiO_3$ thin films grown on LAO (001) substrate were annealed in LPO2 environment at 400 °C to create oxygen vacancies. To vary the density of oxygen vacancies in the samples, the annealing time was controlled to be 0, 7.5, 15, 22.5, 30, 60, 90, 120 min for each sample, respectively.

(2) Electrical transport mechanisms of pristine and oxygen deficient SNO thin films

To investigate the carrier transport mechanisms of pristine and oxygen deficient SNO thin films, we measure the resistance as a function of temperature upon cooling from room temperature to 60K (Fig. S4A). The oxygen deficient SNO was obtained by annealing in LPO2 at 400 °C for 1 h resulting in 6 orders of magnitude increase in resistivity. The resistance of oxygen deficient SNO is beyond the measurement window of the Quantum Design physical properties measurement system (PPMS) below ~200 K. The low temperature transport mechanism of rare-earth nickelate are described by variable range hopping as $R(T) = R_0 \exp{(T_0/T)^p}$, where R_0 is the prefactor, T_0 is the characteristic temperature, p is the exponent relating to the transport mechanism: $p =1$ for activated conduction; $p =1/2$ for variable range hopping with a Coulomb gap near the Fermi level [i.e. Efros-Shklovskii VRH (ES VRH)]; $p =1/4$ for Mott variable range hopping (Mott VRH) of a three dimensional system.

As shown in Fig. S4B, the resistance of pristine SNO in temperature range from 300 K to 60 K is fitted well with the Mott VRH mechanism with $p =1/4$. The characteristic temperature is fitted as $T_0 = T_{Mott}$=5.08×10^5 K. For 3D system, the coherence length ξ of carriers is given by $T_{Mott} = \frac{18}{k_B N(E_f)\xi^3}$, where $N(E_f)$ is the DOS near Fermi level. Taking $N(E_f) = 1.5 \times 10^{18}$ eV^{-1}cm^{-1} (1), the coherence length ξ for pristine SNO sample here is ~6.49 nm. The average hopping distance $R_h =$

$\left(\frac{9\xi}{8\pi k_B TN(E_F)}\right)^{1/4}$ is calculated to be ~15.6 nm at T = 300 K (1, 2). The condition $R_h/\xi > 1$ is satisfied for the Mott VRH fitting.

The resistance of sample containing a large amount of oxygen vacancies is found to be fitted well by the ES VRH mechanism with $p = 1/2$ (Fig. S4C), indicating the emergence of Coulomb gap due to electron correlations. The characteristic temperature is extracted from the fitting as $T_0 = T_{ES} = 1.329 \times 10^5$ K. For the ES VRH mechanism, the coherence length ξ of carriers can be calculated by $T_{ES} = \frac{2.8\,e^2}{4\pi\varepsilon_r\varepsilon_0 k_B \xi}$, where ε_r is the dielectric constant and ε_o is the electric permittivity of the vacuum. Taking ε_r as ~5 (3), the coherence length ξ for oxygen deficient SNO sample shrinks to 0.7 Å which is much smaller than the lattice constant of SNO (~0.38 nm). The average hopping distance $R_h = \frac{1}{4}\left(\frac{2.8e^2\,\xi}{4\pi\varepsilon_r\varepsilon_0 k_B T}\right)^{1/2}$ is calculated to be ~0.37 nm at T = 300 K (4), which satisfies the condition $R_h/\xi > 1$ is required for the ES VRH fitting. The transport analysis thus indicates that the carriers are strongly localized due to oxygen vacancy formation.

(3) Monte Carlo Simulations

To understand the non-linear evolution of the resistivity with annealing time in oxygen deficient thin films (Fig. 2C), we employed an experimentally motivated Monte Carlo simulation to calculate the conductance as a function of charged dopant concentration. The model consists of an $N \times N$ square lattice with hydrogenic atoms placed at each lattice site. At a given Monte Carlo step t, the valence electrons are bound to their respective lattice site via a harmonic potential of the form

$$U_{t,i} = \tfrac{1}{2}\gamma\left(|\vec{u}_{t,i}| - u_0\right)^2,$$

where i is the lattice-site index, $\vec{u}_{t,i}$ the displacement from its respective lattice site, and u_0 is the distance at which the electron achieves its energetic minimum. Additionally, electrons at sites i and j separated by r_{ij} interact via a screened Coulomb potential

$$V_{t,ij}^{sc} = \frac{e^{-k_{t,i}r_{ij}}}{4\pi\varepsilon_0}\frac{q_i q_j}{r_{ij}}\theta(l_{t,i} - r_{ij})$$

with

$$k_{t,i} = \sqrt{\rho_{t,i}} = \frac{1}{l_{t,i}},$$

where $\rho_{t,i}$ is the local charge density and $l_{t,i}$ is the site-dependent cutoff radius. We employ this cutoff as well as the Heaviside step function θ to enforce locality of the interaction, as well as to ease some computational burden. The local charge density is defined as the total charge within the cutoff radius of the previous step divided by the area within the cutoff radius. To start, the cutoff radius ensures only nearest-neighbor interactions; it is updated over the course of the simulation using the local charge density from the previous step.

As such, the Hamiltonian takes the form

$$\mathcal{H}_t = \frac{1}{2}\sum_i \gamma\left(\left|\vec{u}_{t,i}\right| - u_0\right)^2 + \sum_{i,j} V_{t,ij}^{sc}.$$

We allow all of the electrons in the system to move randomly filtered by the Metropolis acceptance/rejection criterion (5). If an electron should gain more energy than some pre-defined E_{trans}, then we say it "transitions" into a conducting state leaving behind a hole of charge +1.0e. This positive charge is included in the local charge density and interacts with the both the valence electrons and the "transitioned" conduction electrons via the screened Coulomb potential. This characteristic of the simulation was included to further encapsulate the percolative behavior seen in the insulator-metal phase transitions of correlated materials (6). Thus, the first term of the Hamiltonian sums over the N^2 lattice sites and the second sums over all pairs of charged particles, both electrons and holes, of which there are $N^2 + N_h$.

To investigate the influence of charged dopants on the conductivity of the systems, we define the dopant concentration, d, as the ratio of the total number of dopants, N_d, to the total number of sites, N^2. For a given concentration d, $d \times N_d$ dopants are placed at lattice sites replacing the hydrogenic atoms, the remaining dopants are placed at random interstitial sites. The interstitial dopants are allowed to move randomly throughout the system with their moves filtered once again by the Metropolis acceptance/rejection criterion. All dopants are included in the local charge density and interact via the screened Coulomb potential; therefore, the second sum in the Hamiltonian is now over all pairs of charged particles: electrons, holes and dopants, of which there are $N^2 - dN_d + N_h + N_d$. Furthermore, as we have removed some hydrogenic atoms from lattice sites and replaced them with dopants, the first sum in the Hamiltonian sums over the remaining $N^2 - dN_d$ hydrogenic atoms.

The workflow for how the simulation is implemented is summarized as follows:

1. Initialize random electron displacements and dopant positions, couple the system to a heat bath at constant temperature T;
2. Each electron and interstitial dopant (if included) attempts a trial move that is passed through a simple Metropolis filter;
3. The energy of each electron is calculated and electrons may transition to conducting states according to the above-mentioned criterion;
   (Performing steps 2 and 3 is known as one Monte Carlo Step (MCS))
4. Total energy and other relevant quantities are gathered;
5. Local electronic density and local cutoff radius are updated;
6. Repeat from 2 until the system has achieved a steady state.

In order to gather data about the change in electrical conductance of the system with respect to input parameters, we define a conductance C_t as:

$$C_t = \frac{1}{N^2 - dN_d}\sum_i s_{t,i} \text{ with } s_i = \begin{cases} 0 & if\ site\ i\ in\ insulating\ state \\ 1 & if\ site\ i\ in\ conducting\ state \end{cases}$$

where the sum is taken over all $N^2 - dN_d$ electrons. Furthermore, we can define a resistance R_t simply as $1 - C_t$ wherein the above defined conductance merely measures the proportion of conducting sites to the total number of sites. This quantity can be used to inform us about changes in material response dependent upon different initial parameters. We define a steady state of the system to be one where the conductance does not appreciably change over times scales of ~ 100 MCS.

In the following discussion we use a 50×50 square lattice with a lattice spacing of 1 and periodic boundary conditions with the following values of our parameters across the entire lattice: $k_B T = 30.0$, $E_{trans} = 10.0$, $u_0 = 0.5$, $\gamma = 1.0$, along with a dopant charge of +2.0e.

Figure S3 shows a nonlinear dependence of the resistance as a function of dopant concentration, where the dopant charge is +2.0e. The dopants are acting as electron traps where they lower the energy of nearby electrons and increase the energy requirement to transition to the conducting state. As more dopants are added, this effect increases, further suppressing the conductivity. 3D versions of the simulation have been performed with $N \times N \times M$ systems where $M \approx 0.10N$, and no qualitative differences could be discerned, further validating the results of the 2D model. This would indicate that the inclusion of the charged dopants advances the percolative evolution of such a phase transition.

(4) Solid-state oxygen-deficient perovskite nickelate resistive switches

We designed a proof-of-concept solid-state resistive switch utilizing an oxygen-deficient NdNiO$_{3-\delta}$ functional layer; and the schematic is shown in Fig. S14A. Pd and FTO serve as top and bottom electrodes. Oxygen vacancies were created in the NdNiO$_3$ thin film by LPO2 annealing at 400°C for 40min. During testing, FTO was grounded and a voltage pulse was applied to the Pd top electrode. In Fig. S14B and C, we propose the working principle for the NdNiO$_{3-\delta}$ switch. Under negative electric field, oxygen vacancies are redistributed and migrate towards the top electrode. With the accumulation of a high density of oxygen vacancies near the top electrode, NdNiO$_{3-\delta}$ near top electrode becomes insulating and possesses large energy gap, leading to a higher Schottky barrier with the Pd electrode contact. As a result, the resistance of the devices rises under a negative electric field. By reversing the polarity of the external field, oxygen vacancies are pushed away from top Pd electrode, resulting in a more conducting state of NdNiO$_{3-\delta}$ with narrower band gap. The Schottky barrier between Pd and NdNiO$_{3-\delta}$ decreases. As a result, the device becomes more conductive.

We compare the resistance modulation of devices made from pristine NdNiO$_3$ and oxygen deficient NdNiO$_{3-\delta}$ under successive negative (-3V for 1s) and positive (+3V for 1s) voltage pulses (Fig. S14D). The resistance after each voltage pulse was recorded. It is observed that compared with pristine NdNiO$_3$ devices, the oxygen deficient devices show an obvious modulation of resistance after the voltage pulse was applied. Under negative bias, the resistance rises quickly, consistent with the proposed mechanism in Fig. S14B. The device saturates at a higher resistance level after 50 pulses, indicating the accumulation of oxygen vacancies near the Pd/NdNiO$_{3-\delta}$ interface region. The resistance of the device recovers back to original state after reversing the bias

field, suggesting the proposed picture in Fig. S14C which indicates the depletion of oxygen vacancies near the interface.

We also track the resistance modulation as a function of magnitude of the voltage pulse, finding a monotonic decrease of resistance modulation with reducing voltage (Fig. S14E). Moreover, a linear scaling behavior is found between the resistance modulation and the applied energy (V^2t). For the endurance test, the switching was defined as a -2V, 2s pulse for set and +2V, 2s pulse for reset (Fig. S14E). The resistance of cell was read by a small voltage of -0.05V. This NdNiO$_{3-\delta}$ device is found to be stable over 10^4 cycles.
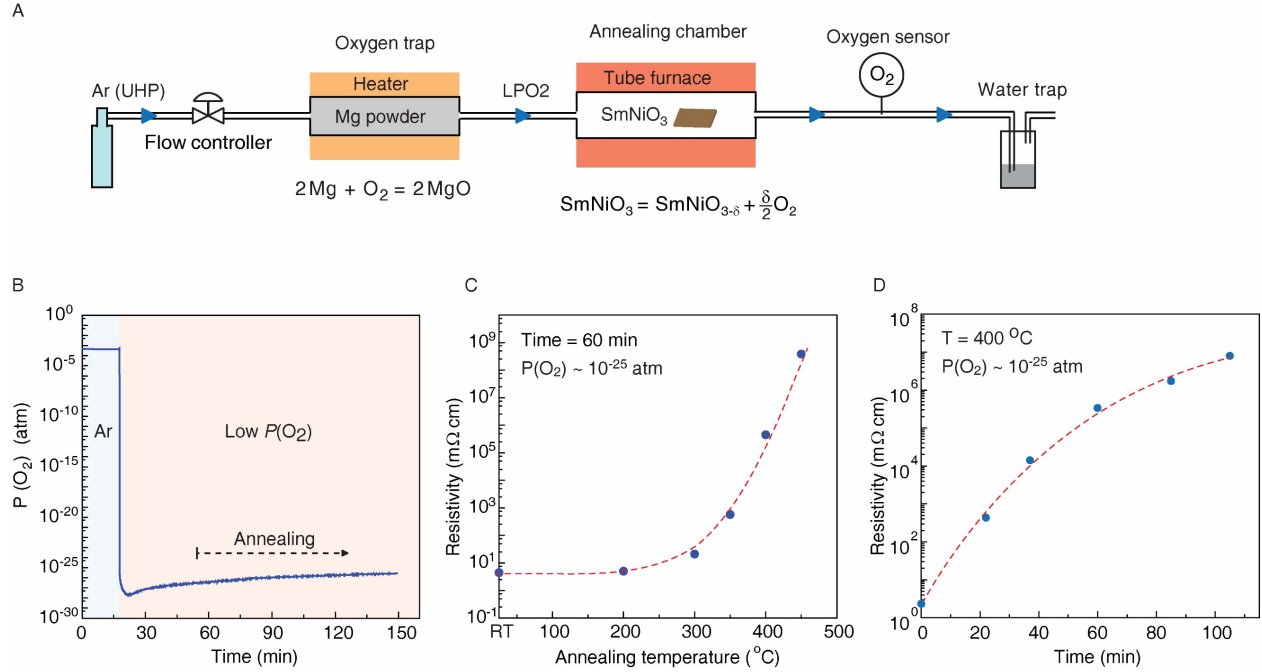
Fig. S1. Schematic of experimental setup to generate the low oxygen partial pressure (LPO2) environment and post-annealing of nickelate thin films. (**A**) Experimental setup for creating LPO2 environment. The trace amount of oxygen in ultra-high purity (UHP) argon gas is filtered by a home-built Mg trap utilizing the strong oxidation reaction between Mg powder and O_2. Then, the SNO thin films are annealed in a tube furnace with constant flow of extremely low $P(O_2)$ Ar gas to introduce oxygen vacancies. During annealing the oxygen partial pressure is monitored by a zirconia-based oxygen sensor. At the end, a water trap is utilized to prevent the oxygen contamination from outside. (**B**) Representative oxygen partial pressure of the system monitored by the oxygen sensor. When LPO2 is switched ON, the $P(O_2)$ of system can reach as low as ~10^{-26} atm. SNO thin films were annealed after the LPO2 environment is stabilized. At this extremely low $P(O_2)$, oxygen vacancies form at low temperature (~300 ℃) which helps in avoiding structure degradation. (**C**) Temperature dependent resistivity evolution of SNO after annealed in LPO2 for 60 min. The electrical resistivity of SNO shows substantial increase above 300 ℃, indicating the temperature threshold of oxygen vacancy formation in this work. (**D**) Electrical resistivity at room temperature of SNO after annealing in LPO2 environment [$P(O_2)$ ~ 10^{-25} atm] at 400 ℃ for 22, 37, 60, 85, and 105 minutes. With increasing annealing time, the resistivity of SNO thin films increases by nearly seven orders of magnitude, indicating electron localization due to oxygen vacancies.
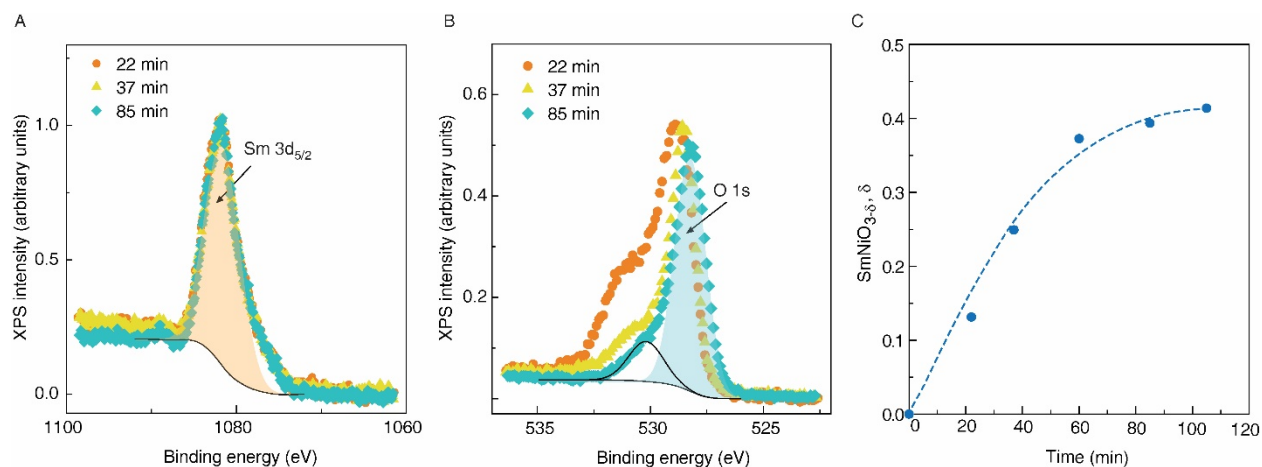
Fig. S2. Oxygen deficiency in SmNiO₃ after annealing in LPO2 environment. Representative XPS spectra of **(A)** Sm $3d_{5/2}$ and **(B)** O $1s$ of $SmNiO_3$ after annealing in LPO2 at 400 °C for 22, 37, and 85 min. The intensities of XPS spectra are normalized to the Sm $3d_{5/2}$ peak of samples. In this work, the oxygen deficient level of SNO after LPO2 annealing was estimated by taking the ratio of the effective peak area of Sm $3d_{5/2}$ (orange region, constant for all annealing times) and O $1s$ (for example shown by the blue region for an annealing time of 85 min) after the background is subtracted. The broad XPS peak located at the higher binding energy of O $1s$ is a result of surface contamination such as hydroxide groups and is therefore not considered in the analysis. **(C)** Estimated oxygen deficiency level of $SmNiO_{3-\delta}$ as a function of annealing time in LPO2 environment at 400 °C.
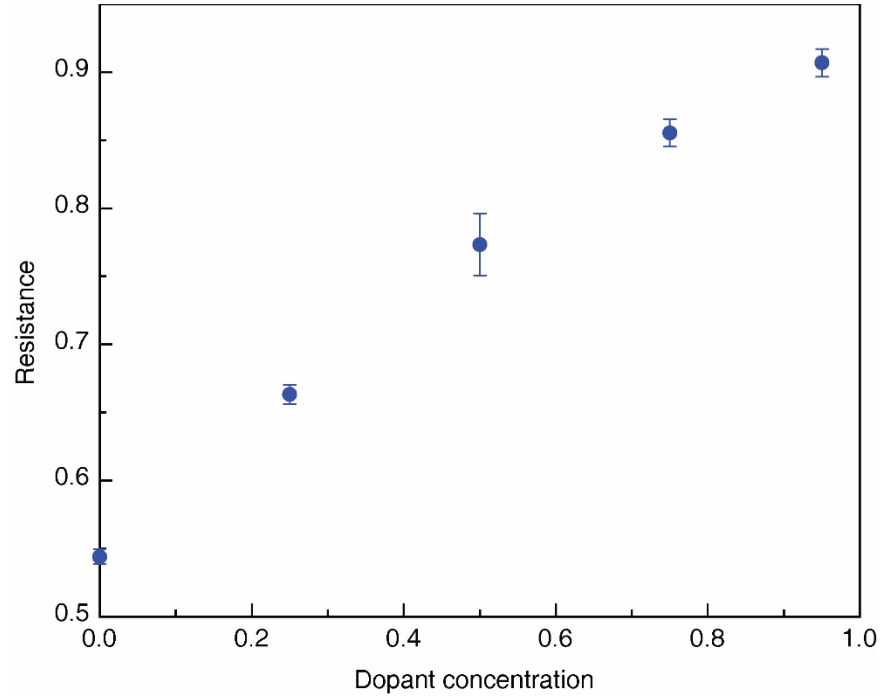
Fig. S3. Monte Carlo simulations of resistance of a correlated system as a function of dopant concentration at $k_B T/E_{trans}$=3.0. The dopant charge is +2.0e. The Monte Carlo step is 400.
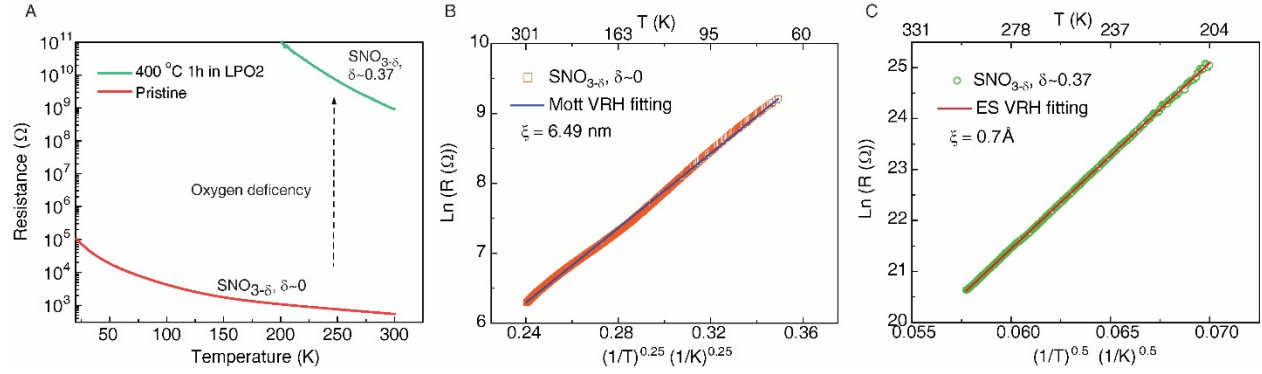
Fig. S4. Electrical transport mechanisms in representative pristine and oxygen deficient SNO thin films. (A) Low temperature resistance − temperature curves of pristine ($\delta \sim 0$) and oxygen deficient ($\delta \sim 0.37$) SNO thin films. The oxygen deficient SNO was obtained by annealing in LPO2 at 400 °C for 1 h. **(B)** The resistance of pristine SNO in the temperature range from 300 K to 60 K, with fit to Mott variable range hopping mechanism (Mott VRH) with the coherence length $\xi \sim$ 6.49 nm [Supplementary Text (2)]. **(C)** The resistance of oxygen deficient SNO in the temperature range from 300 K to 200 K, with fit to Efros-Shklovskii variable range hopping (ES VRH) mechanism with the coherence length $\xi \sim 0.7$ Å.
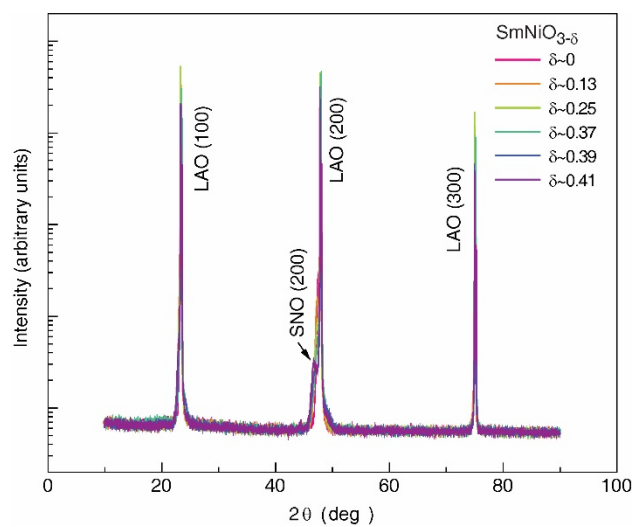
Fig. S5. Wide range X-ray diffraction profile of SNO thin films after annealing in LPO2 at 400 ºC. With δ approaching ~ 0.42, no new diffraction peaks appear, indicating the preservation of perovskite structure within this regime.
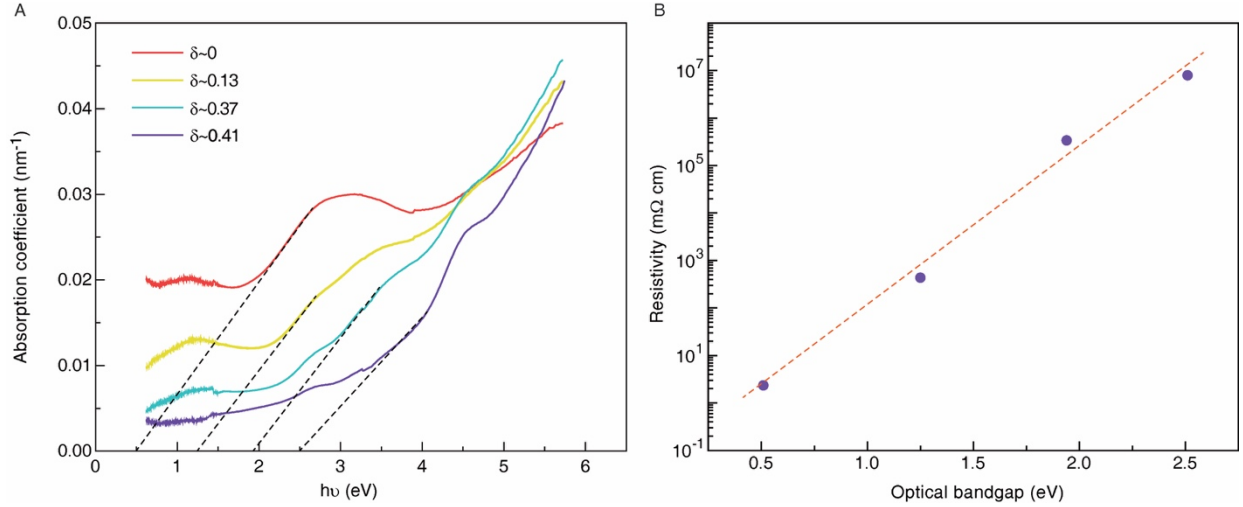
Fig. S6. Optical bandgap of SNO thin films after LPO2 annealing at 400°C. (A) The absorption coefficient as a function of photon energy (*h*ν) for oxygen deficient SNO thin films calculated from transmittance spectrum shown in Fig. 3(B). An optical bandgap of ~2.5 eV can be obtained in oxygen deficient SNO thin films. **(B)** Correlation between electrical resistivity and optical bandgap of oxygen deficient SNO, demonstrating a semiconductor-like exponential relationship. Fitting the observed scaling behavior between the resistivity, ρ, and the band gap, E_g, with $\rho = \rho_0 e^{(\beta E_g)}$ yields $\beta \sim 7.75$ eV$^{-1} \approx (5k_BT)^{-1}$, which is smaller than the typical semiconductor scaling factor of $(2k_BT)^{-1}$. Such a deviation from traditional semiconductor behavior indicates the coexistence of insulating and metallic regions in the oxygen deficient SNO as the annealing process evolves.
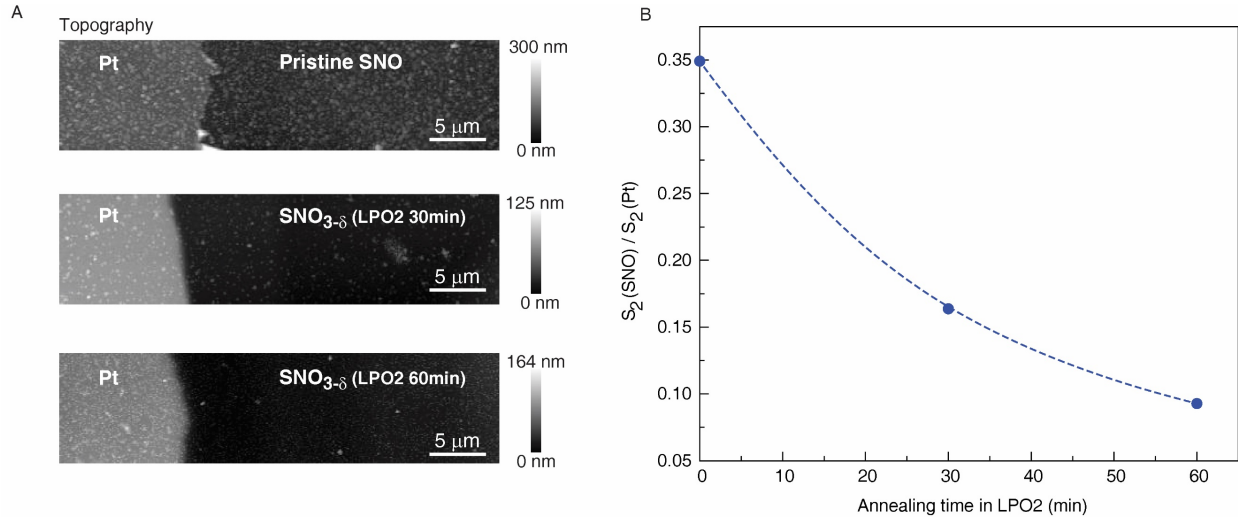
Fig. S7. Supplementary information on midinfrared (λ=10.5 µm) nano-Images of oxygen deficient SNO samples. (A) Topography of SNO thin films after LPO2 annealing at 400 °C. A Pt electrode was deposited on top of the SNO thin film after LPO2 annealing as a reference. **(B)** Normalized second harmonic near field amplitude s_2 (SNO)/ s_2 (Pt) as a function of annealing time in LPO2 environment at 400 °C.
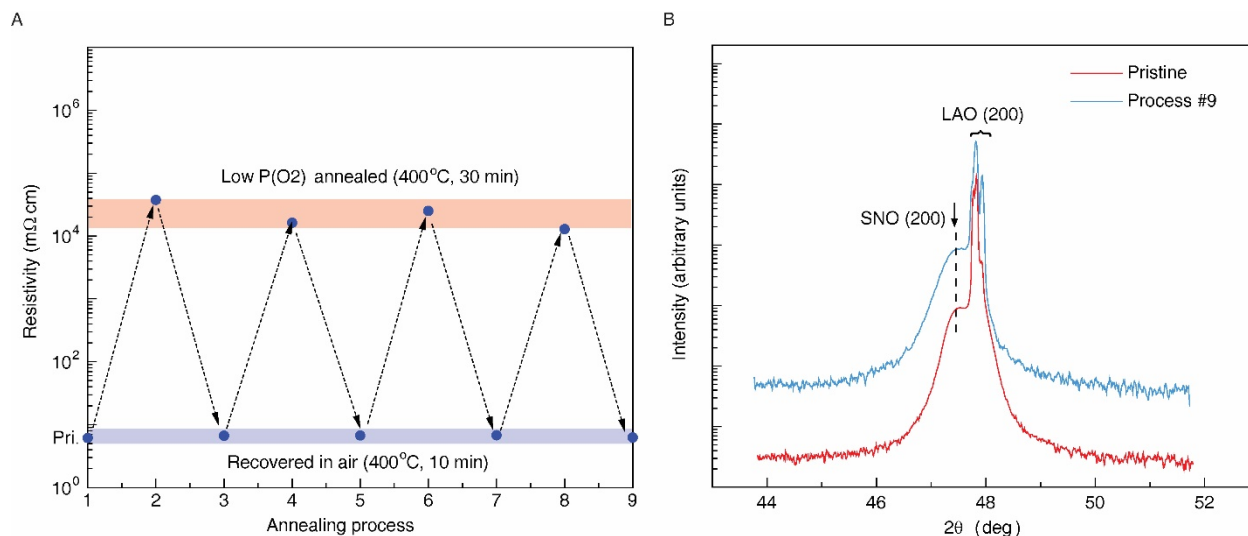
Fig. S8. Reversibility of SNO resistivity after annealing in LPO2 at 400 ºC. (A) Electrical resistivity of SNO after annealing at 400 ºC in LPO2 and air subsequently. Over multiple cycles the resistivity of LPO2 annealed SNO recovers back to the original state after exposing to air for 10 min at 400 ºC. **(B)** The X-ray diffraction profile of SNO after multiple annealing processes (#9) has almost the same form as that of pristine state, confirming the reversibility of SNO upon oxygen vacancy formation within the stability window.
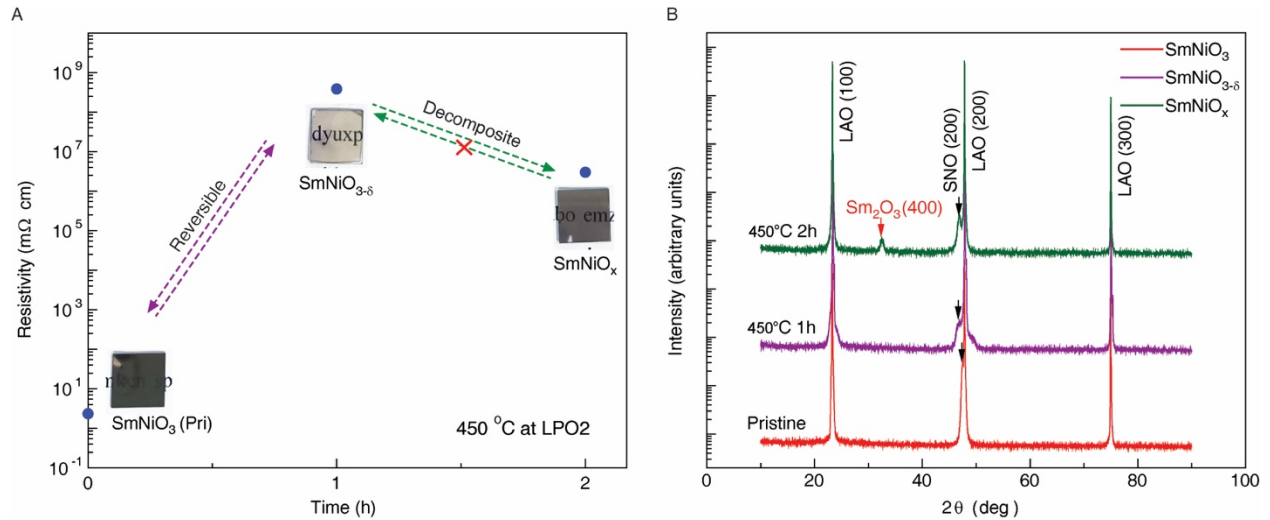
Fig. S9. Stability limit of perovskite structured SNO in LPO2 environment. (**A** and **B**) Electrical resistivity and X-ray diffraction curves of SNO after annealing in LPO2 at a higher temperature (450 °C), showing the stability limit of perovskite SNO. With an annealing time of 1 h, the SNO sample becomes transparent and the resistivity increases by more than seven orders of magnitude (A); and no phase decomposition occurs, as observed in its X-ray diffraction curve (B). Within this regime, the oxygen deficient SNO retains the perovskite crystal framework and is reversible upon annealing in oxygen gas. By increasing the annealing time to 2 h in 450 °C, the resistivity and transparency of SNO drops (A), the X-ray diffraction curve of which show new peak matching the Sm_2O_3 (400) diffraction plane (B). In this regime, phase decomposition occurs in oxygen deficient SNO. As a result, the sample becomes irreversible allowing us to identify a robust experimental set of conditions for in-depth studies on samples using multiple techniques.
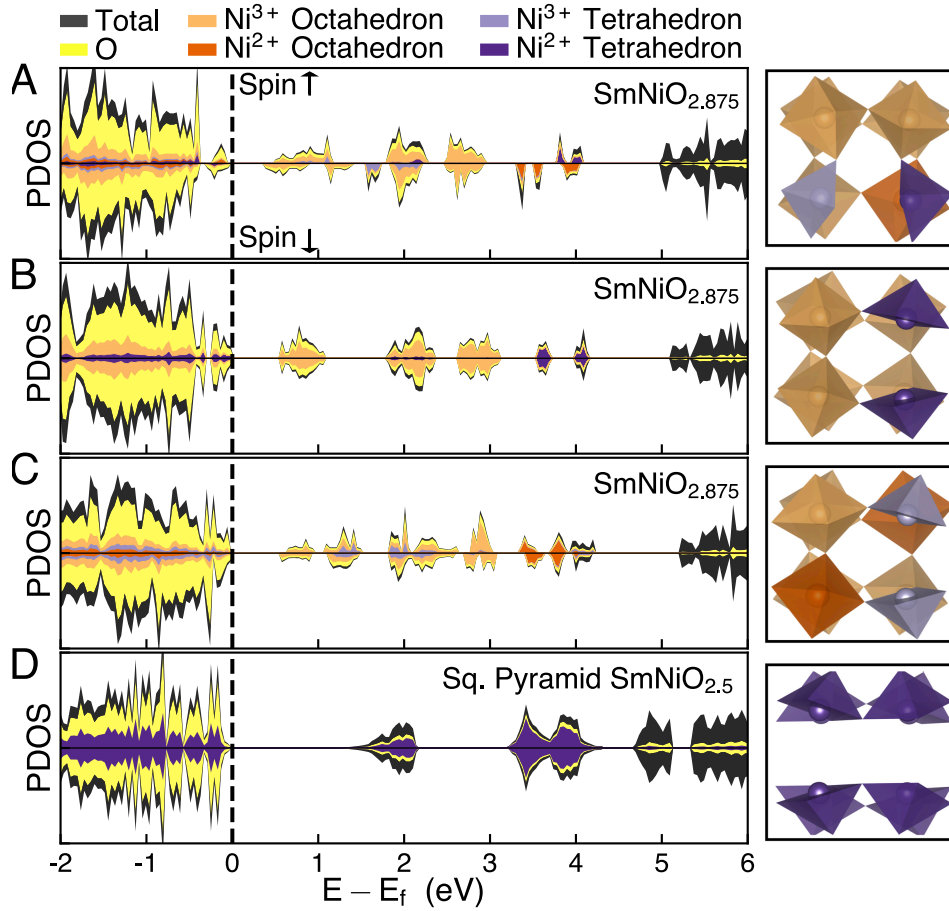
Fig. S10. Additional density of states of oxygen deficient SNO. (A)-(C) Density of states (DOS) of SNO$_{2.875}$ with G-type (checkerboard) magnetic ordering in dark gray. Projected DOS (PDOS) of oxygen in yellow and nickel in orange or purple depending on the coordination and valence. (A) Electrons localized on one square pyramid and octahedron with oxygen vacancy in ab-plane. (B) Electrons localized on two square pyramids with apical oxygen vacancy. (C) Electrons localized on two octahedra with apical oxygen vacancy. (D) DOS of SNO$_{2.5}$ with all apical oxygen vacancies resulting in Ni^{2+} only in NiO$_5$ square pyramids. The unoccupied states between 1.5 to 2.5 eV are dominated by states localized on the oxygen vacanies. Corresponding structure of supercell shown in the left column, showing only the nickel-oxygen polyhedra (nickel centered with oxygens at the vertices) and omitting the samarium atoms for clarity. Polyhedra color correspond to the colored PDOS.
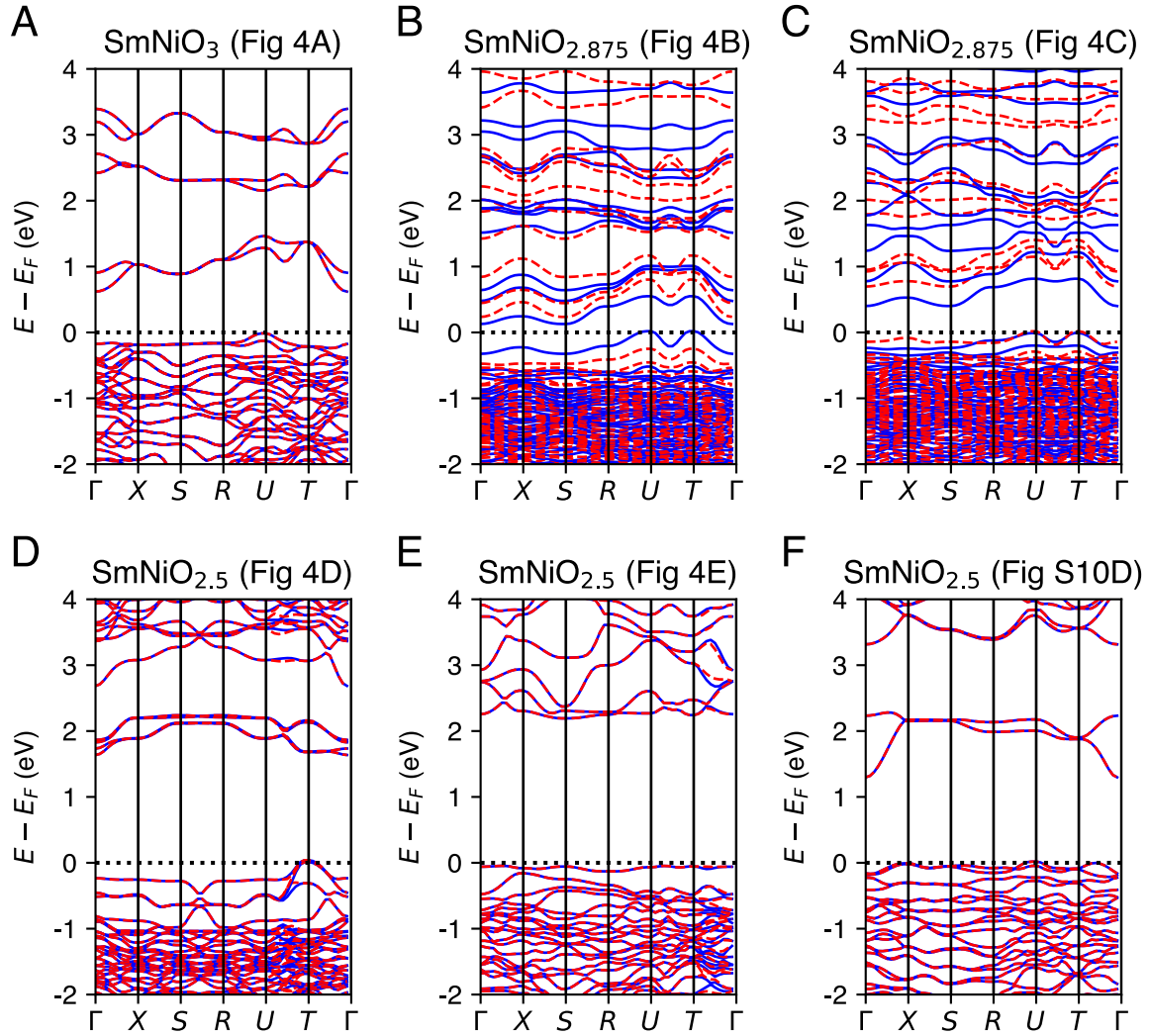
Fig. S11. Band structure of oxygen deficient SNO. (A) Band structure of pristine SNO corresponding to density of states (DOS) in Fig. 4A. **(B)&(C)** Band structure of SNO$_{2.875}$ corresponding to DOS in Fig. 4B&C. The degeneracy breaking is a result from the symmetry lowering that occurs when introducing an oxygen vacancy and allowing the ionic positions to relax. **(D)-(F)** Band structure of SNO$_{2.5}$ corresponding to DOS in Fig. 4D&E and Fig. S10D, respectively. The spin-up bands are shown in solid blue and the spin-down bands are shown in dashed red. The high-symmetry k-points are defined with respect to the *Pbnm* unit cell (a $\sqrt{2} \times \sqrt{2} \times 2$ supercell of the perovskite primitive cell*)* and the path through k-space was chosen to be the same in all cases.
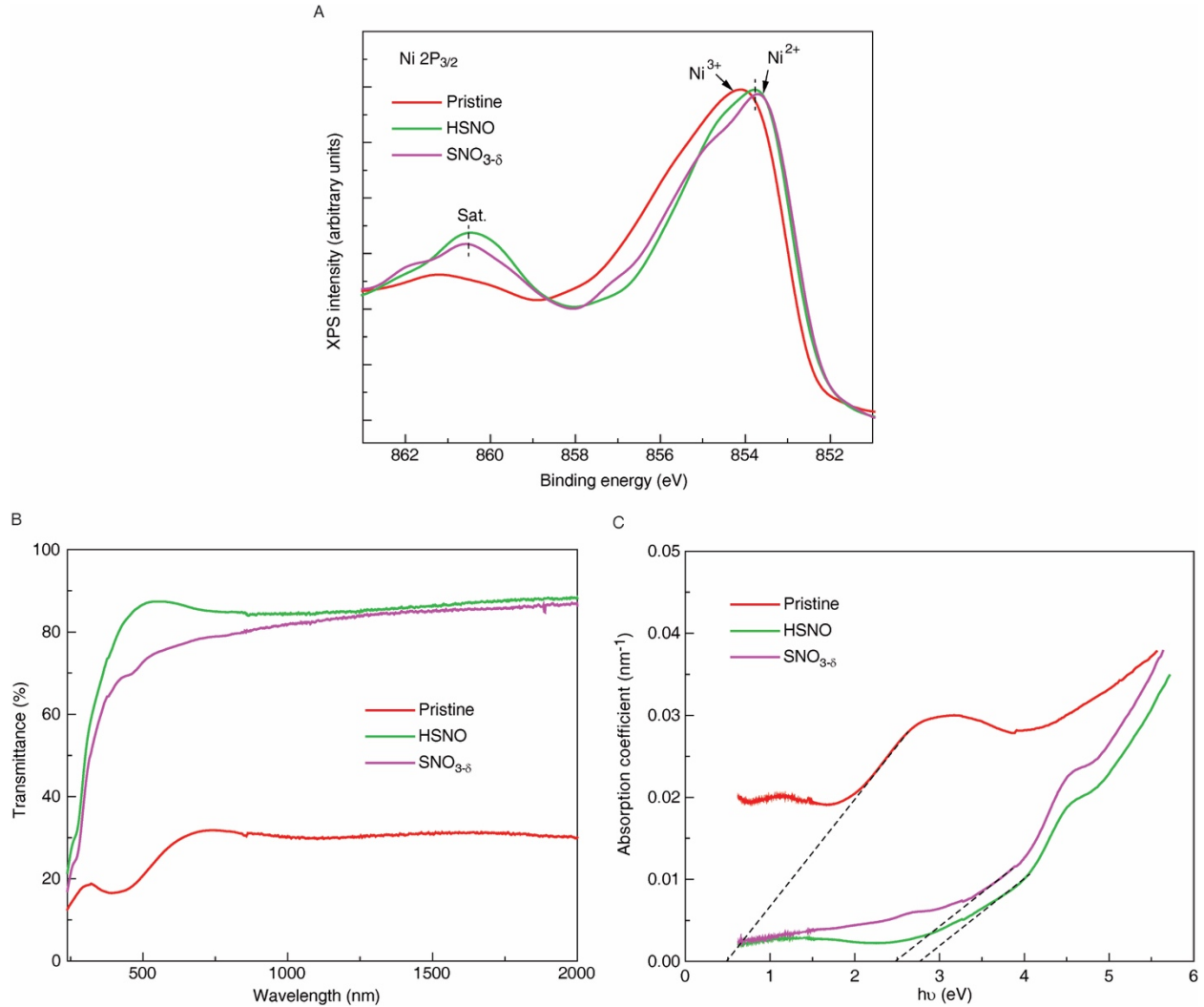
Fig. S12. Comparison of optical properties of hydrogenated SmNiO₃ (HSNO) and oxygen deficient SmNiO₃₋ᵨ (SNO₃₋ᵨ). (**A**) Ni $2p_{3/2}$ XPS spectrum of HSNO and SNO$_{3-\delta}$ thin films. Compared with the XPS spectrum of pristine SNO, the Ni $2p_{3/2}$ photoemission peak and satellite peak (Sat.) of HSNO and SNO$_{3-\delta}$ show almost identical shift towards lower binding energy, indicating the existence of similar amount of Ni^{2+} in both samples. (**B**) Optical transmittance of HSNO and SNO$_{3-\delta}$. Though both samples become more transparent after treatment, the HSNO sample possesses higher transmittance than SNO$_{3-\delta}$ over the whole measured wavelength range. Their difference becomes more obvious in the visible wavelength region. (**C**) The absorption coefficient of HSNO and SNO$_{3-\delta}$ calculated from (B). A larger optical bandgap appears in HSNO than that in SNO$_{3-\delta}$, which is consistent with the theoretical calculations and demonstrates the role of crystal filed splitting in oxygen deficient SNO.
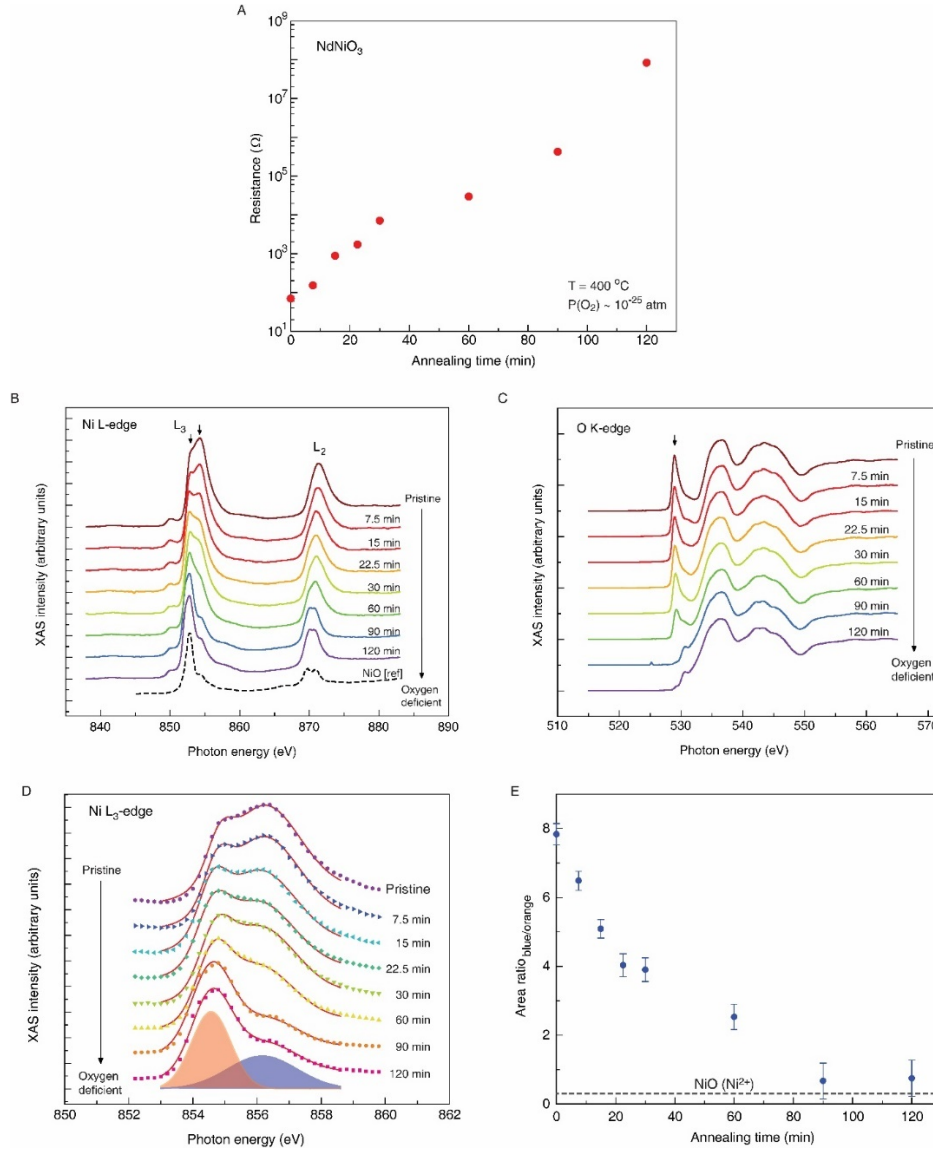
Fig. S13. Quantitative analysis of X-ray absorption (XAS) spectra of NdNiO₃ with increasing oxygen deficiency. (A) Electrical resistance of NdNiO₃ (NNO) thin film after annealing in LPO2 environment at 400 °C. A substantial increase of the electrical resistance occurs in oxygen-deficient NNO thin films after annealing, consistent with the observations in SNO thin films (Fig. 2B). The changes in the properties of both oxygen deficient SNO and NNO thin films are governed by the same general mechanism. **(B)** Ni-L edge and **(C)** O-K edge x-ray absorption spectra at room temperature on series of NdNiO₃ films with increasing oxygen vacancy concentration. The spectra are vertically shifted for clarity. The Ni L-edge spectrum of NiO, the valence state of which is Ni^{2+}, was extracted from Reference (7).**(D)** Two Gaussian fitting on the Ni L₃-edge XAS spectra of oxygen deficient NNO. The individual gaussian components centered at ~854.5 eV (orange) and ~856 eV (blue) for NNO annealed for 120 minutes are shown at the bottom. **(E)** The area ratio of two fitted gaussian components (blue/orange from (D)) as a function of annealing time. The grey dashed line is the area ratio (~0.31) extracted from the XAS spectrum of NiO reported in Reference (7) by the same method.

20
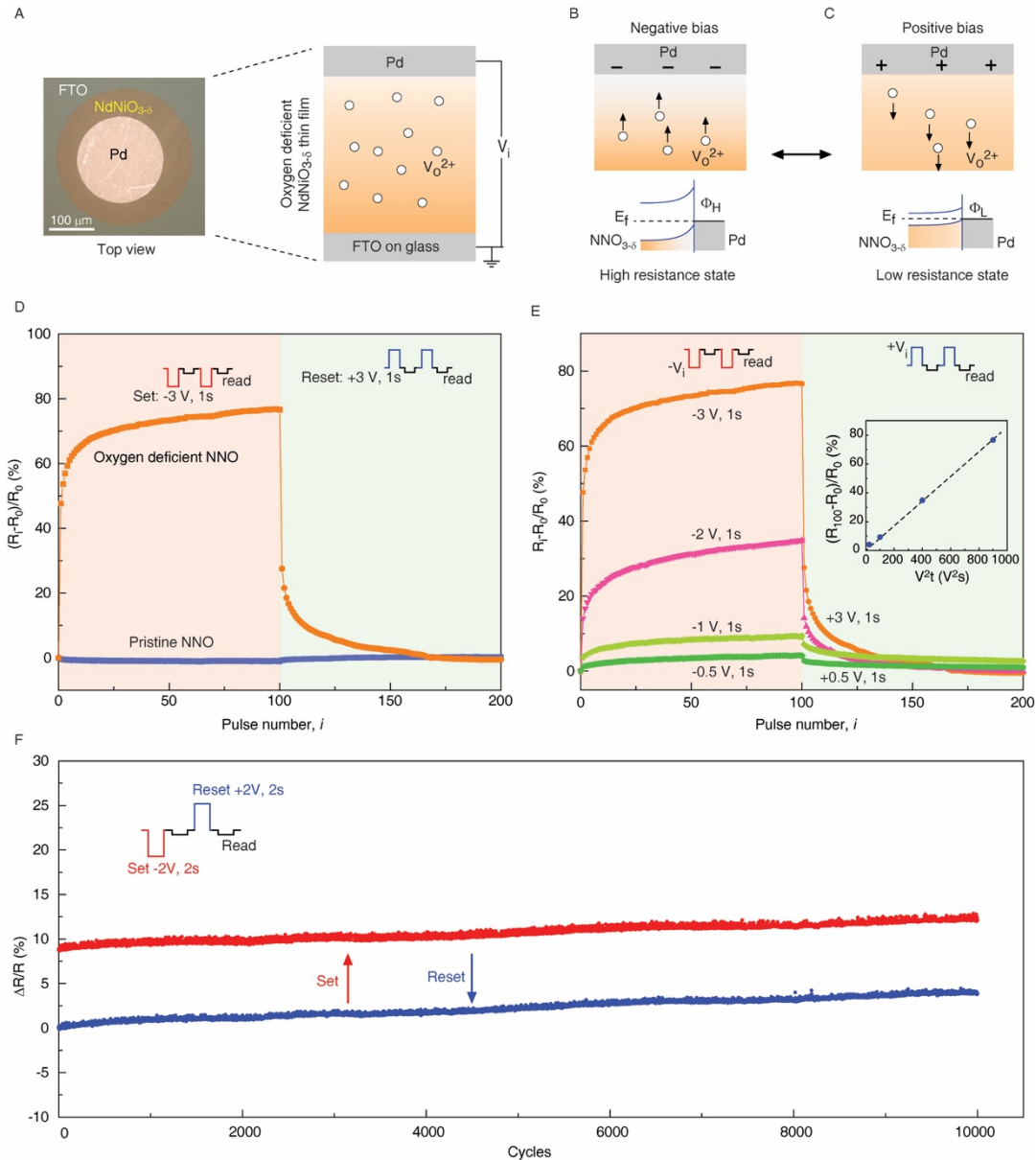
Fig. S14. Solid-state oxygen-deficient perovskite nickelate switches. (A) Schematic of vertical solid-state switch utilizing an oxygen-deficient $NdNiO_{3-\delta}$ functional layer. **(B)** and **(C)** The high- and low-resistance state of the $NdNiO_{3-\delta}$ memristor, respectively. The resistance is modulated by redistributing the oxygen vacancies using an electric field [Supplementary Text (4)]. **(D)** Comparing the resistance modulation of devices made from pristine $NdNiO_3$ and oxygen deficient $NdNiO_{3-\delta}$ under successive negative (-3V for 1s) and positive (+3V for 1s) voltage pulses. (**E**) Resistance modulation as a function of magnitude of the voltage pulse, showing a monotonic decrease of resistance modulation with reducing voltage. Moreover, a linear scaling behavior is found between the resistance modulation and the applied energy (V^2t). (**F**) Endurance results of oxygen deficient $NdNiO_{3-\delta}$ device. The switching was defined as a -2V, 2s pulse for set and +2V, 2s pulse for reset. The resistance of cell was read by a small voltage of -0.05V. Stability over 10^4 cycles is observed.

Table S1. Total energy of geometries in DFT calculations. All G-type (checkerboard) magnetic ordering

Composition	Description	Figure	Energy (eV/Ni)
SmNiO$_{2.875}$	Oxygen vacancy in ab-plane; electron localized on two NiO$_5$ square pyramids	4B	-32.843
	Oxygen vacancy in ab-plane; electron localized on two NiO$_6$ octahedra	4C	-32.867
	Oxygen vacancy in ab-plane; electron localized on one NiO$_5$ square pyramid & one NiO$_6$ octahedron	S10A	-32.856
	Apical oxygen vacancy; electron localized on two NiO$_5$ square pyramids	S10B	-32.812
	Apical oxygen vacancy; electron localized on two NiO$_6$ octahedra	S10C	-32.836
SmNiO$_{2.5}$	Brownmillerite (like SrCoO$_{2.5}$)	4D	-30.613
	NiO$_4$ Chains (like LaNiO$_{2.5}$)	4E	-30.522
	NiO$_5$ Square pyramids (like BaYMn$_2$O$_5$)	S10D	-30.362

References

1. Ramadoss K, et al. (2016) Sign reversal of magnetoresistance in a perovskite nickelate by electron doping. *Phys Rev B* 94(23):235124.

2. Mott NF, Davis EA (1979) *Electronic Processes in Non-Crystalline Materials* (Clarendon Press, Oxford). 2nd Ed.

3. Shi J, Zhou Y, Ramanathan S (2014) Colossal resistance switching and band gap modulation in a perovskite nickelate by electron doping. *Nat Commun* 5(1):4860.

4. Efros AL, Shklovskii BI Coulomb gap and low temperature conductivity of disordered systems. *J Phys C Solid State Phys* 8:L49.

5. Metropolis N, Rosenbluth AW, Rosenbluth MN, Teller AH, Teller E (1953) Equation of State Calculations by Fast Computing Machines. *J Chem Phys* 21(6):1087–1092.

6. Abate Y, et al. (2015) Control of plasmonic nanoantennas by reversible metal-insulator transition. *Sci Rep* 5:13997.

7. Medarde M, et al. (1992) $RNiO_3$ perovskites (R=Pr,Nd): Nickel valence and the metal-insulator transition investigated by x-ray-absorption spectroscopy. *Phys Rev B* 46(23):14975–14984.